submitted to *Geophys. J. Int.*

Bayesian waveform-based calibration of high-pressure acoustic emission systems with ball drop measurements

Chen Gu[1], Ulrich Mok[1], Youssef M. Marzouk[2], Germán A Prieto Gomez[3], Farrokh Sheibani[1], J. Brian Evans[1], and Bradford H. Hager[1]

[1] *Earth Resources Laboratory, Department of Earth, Atmospheric, and Planetary Sciences, Massachusetts Institute of Technology, Cambridge, MA* 02139*, USA. Email: guchch@mit.edu*

[2] *Aerospace Computational Design Laboratory, Department of Aeronautics and Astronautics Massachusetts Institute of Technology, Cambridge, MA* 02139*, USA.*

[3] *Departamento de Geociencias, Universidad Nacional de Colombia, Bogotá, Colombia.*

SUMMARY

Acoustic emission (AE) is a widely used technology to study source mechanisms and material properties during high-pressure rock failure experiments. It is important to understand the physical quantity that acoustic emission sensors measure, as well as their response as a function of frequency. This study calibrates the newly built AE system in the MIT Rock Physics Lab using a ball-bouncing system. Full waveforms of multi-bounce events due to ball drops are used to infer the transfer function of Lead-Zirconate-Titanate (PZT) sensors in high-pressure environments. The uncertainty of sensor transfer functions is quantified using a waveform-based Bayesian algorithm. The quantification of $in\ situ$ sensor transfer functions makes it possible to apply full waveform analysis for acoustic emissions at high pressures.

Key words: acoustic emission, ball bouncing, sensor calibration, uncertainty quantification

1 INTRODUCTION

The history of acoustic emissions (AEs) goes back to the middle of the 20th century, before the term "AE" was created in the work of Schofield (1961). Obert & Duvall (1942) first detected subaudible noises emitted from rock under compression and attributed these signals to microfractures in the rock. Kaiser (1950) recorded signals from the tensile specimens of metallic materials. Since the 1960's, much subsequent work has contributed to the development of AE techniques, which have been applied to diverse engineering and scientific problems (Drouillard 1987, 1996; Grosse & Ohtsu 2008).

AEs are useful tools to study the source mechanisms of "labquakes" and the 3-dimensional structure of the samples under diverse fracturing experimental conditions (Pettitt 1998; Schofield 1961; Ojala et al. 2004; Graham et al. 2010; Stanchits et al. 2011; W Goebel et al. 2013; Fu et al. 2015; Hampton et al. 2015; Goodfellow et al. 2015; Li & Einstein 2017). However, it is very difficult to use full waveforms of AEs to infer AE source physics and sample structures, because AE amplitudes are affected by many factors (e.g., sensor coupling, frequency-response of sensors, or incidence angle of ray paths) not related to the AE source or path effects. To determine the real physical meanings of the recorded AEs, the calibration of their amplitudes is needed.

McLaskey & Glaser (2012) performed AE sensor calibration tests on a thick plate with two calibration sources (ball impact and glass capillary fracture) to estimate instrument response functions. Ono (2016) demonstrated detailed sensor calibration methods, including face-to-face, laser interferometry, Hill-Adams equation, and tri-transducer methods. Yoshimitsu et al. (2016) combined laser interferometry observations and a finite difference modeling method to characterize full waveforms from a circular-shaped transducer source through a cylindrical sample. However, these calibration methods only work under ambient conditions, and not within a pressure vessel where rock physics experiments are sometimes carried out. To calibrate the AE amplitudes under high-pressure conditions, Kwiatek et al. (2014) proposed an $in\ situ$ Ultrasonic Transmission Calibration (UTC) method to correct relative amplitudes under high pressure. McLaskey et al. (2015) developed a technique to calibrate a high-pressure AE system using $in\ situ$ ball impact as a reference source. This design enabled the determination of absolute source parameters with an $in\ situ$ accelerometer.

This study aims to advance these measurements further by quantifying the uncertainty of sensor transfer functions using a waveform-based Bayesian algorithm. Instead of using the waveform of one ball bounce, this work is able to use waveforms of multi-bounce events. The quantification of an $in\ situ$ sensor transfer function makes it possible to apply full waveform analysis for acoustic emissions. The method is tested using the newly built AE system of the MIT Rock Physics Laboratory.

2 METHODOLOGY

2.1 Experimental Setup and AE Data

The ball drop apparatus to conduct the $in\ situ$ ball drop experiment is shown in Figure 1. A steel ball (radius $R_1 = 3.18\ mm$) placed in a tube is lifted to the top by air blown into the tube. After the air is cut off, the ball drops and hits the surface of a titanium cylinder (marked as "sample" in Figure 1), bouncing a few times. The diameter of the titanium cylinder is 46.1 mm and the length is 73.7 mm. Sixteen (16) Lead Zirconate Titanate (PZT) sensors are attached to the surface of the titanium cylinder (Figure 2). We stack a nonpolarized PZT piezoceramic disk, a polarized PZT piezoceramic disk, and a titanium disk adapter together to make one sensor. The diameters of the polarized and nonpolarized PZT piezoceramic disks are 5.00 mm and the thicknesses are 5.08 mm. The resonance frequency is 1MHz. The titanium disk adapter has a diameter of 5.00 mm and a thickness of 4.00 mm. The side of the titanium disk adapter contacting the polarized PZT piezoceramic disk is machined to be flat, and the other side contacting the cylindrical sample is machined to be concave, to better fit the curved cylindrical side surface. The ball drop experiment is conducted at a confining pressure of 30 MPa and a differential pressure of 10 MPa.

The AE data are continuously recorded and streamed to a hard drive at a sampling rate of 12.5 MHz, preprocessed by the STA/LTA algorithm to detect events due to ball bounces (Swindell & Snell 1977; McEvilly & Majer 1982; Earle & Shearer 1994). The truncated waveforms of the first and second bounces from 16 sensors due to one ball drop experiment are shown in Figure 2. We implement the Akaike information criterion (AIC) algorithm to automatically pick the P arrival time t_1^j for the truncated waveforms of the first bouncing event (Maeda 1985; Kurz et al. 2005). Then we align the waveforms from the later bounces and the first bounce by cross-correlation. An example of continuous waveforms containing the first three bouncing events of sensor 16 is shown in Figure 3(a). The aligned waveforms of three bouncing events are shown in Figure 3(b). The absolute P arrival time t_k^j of the kth bouncing event can be calculated by adding the time lag between the waveforms of the first and the kth bouncing event to t_1^j. The bouncing time interval for all bounces can be represented by

$$\boldsymbol{\delta t}^j = [t_2^j - t_1^j, t_3^j - t_2^j, \ldots, t_{k+1}^j - t_k^j, \ldots, t_n^j - t_{n-1}^j], \tag{1}$$

where t_k^j is the absolute time of the P arrival of the kth event at sensor j, and n is the total number of bounces.

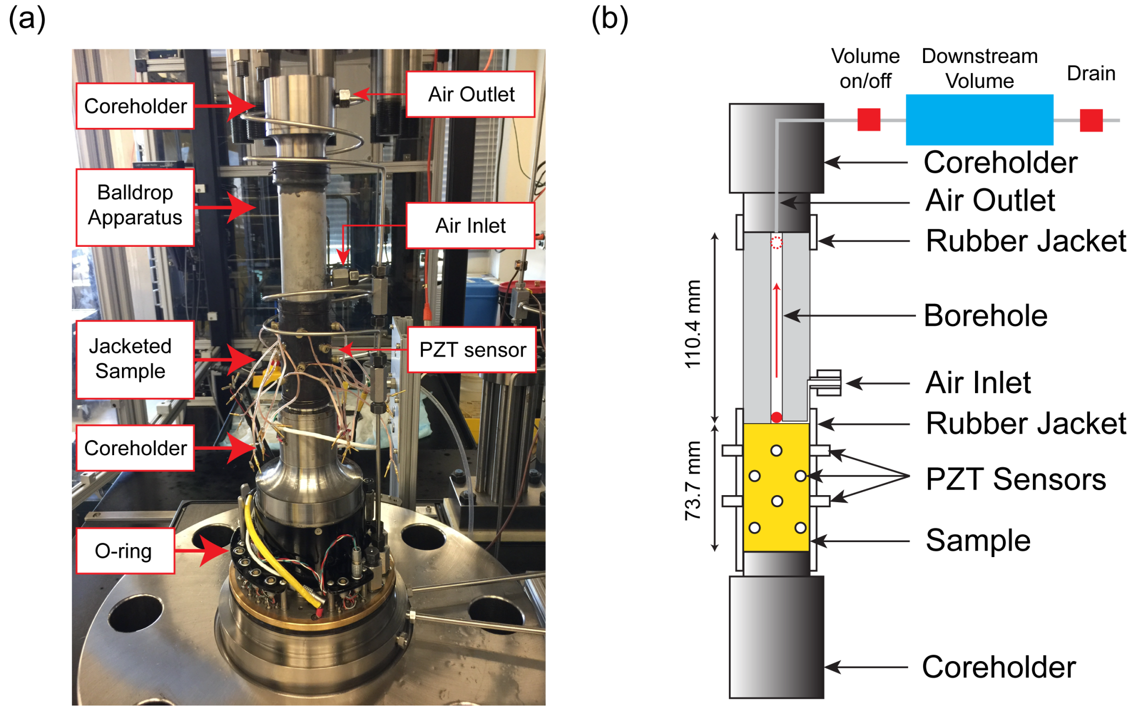

Figure 1. (a) Photo of sample assembly before closing the pressure vessel. (b) Schematic of cross-section of the ball drop apparatus and the instrumented sample.

2.2 Bouncing time and waveform modeling

To model the time interval between bounces, we first assume that after each bounce, the rebound velocity decreases to a (rebound coefficient) of the incident velocity; then the velocity after the kth bounce is

$$v_k = a^k v_0. \tag{2}$$

The time interval between the kth and the $(k-1)$th bounce is

$$\hat{t_k^j} - \hat{t_{k-1}^j} = \frac{2v_k}{g} = \frac{2a^n v_0}{g}, \tag{3}$$

where g is the acceleration of gravity.

The bouncing time interval $\boldsymbol{\delta t_m} = [\hat{t_1} - \hat{t_0}, \hat{t_2} - \hat{t_1}, \ldots, \hat{t_n} - \hat{t_n}]$ can be estimated as

$$\boldsymbol{\delta t_m} = \left[\frac{2av_0}{g}, \frac{2a^2v_0}{g}, \ldots, \frac{2a^n v_0}{g}\right]. \tag{4}$$

Considering noise perturbation $\boldsymbol{e_t^j}$, the bouncing time interval data $\boldsymbol{\delta t}$ is represented as

$$\boldsymbol{\delta t} = \boldsymbol{\delta t_m} + \boldsymbol{e_t^j}. \tag{5}$$

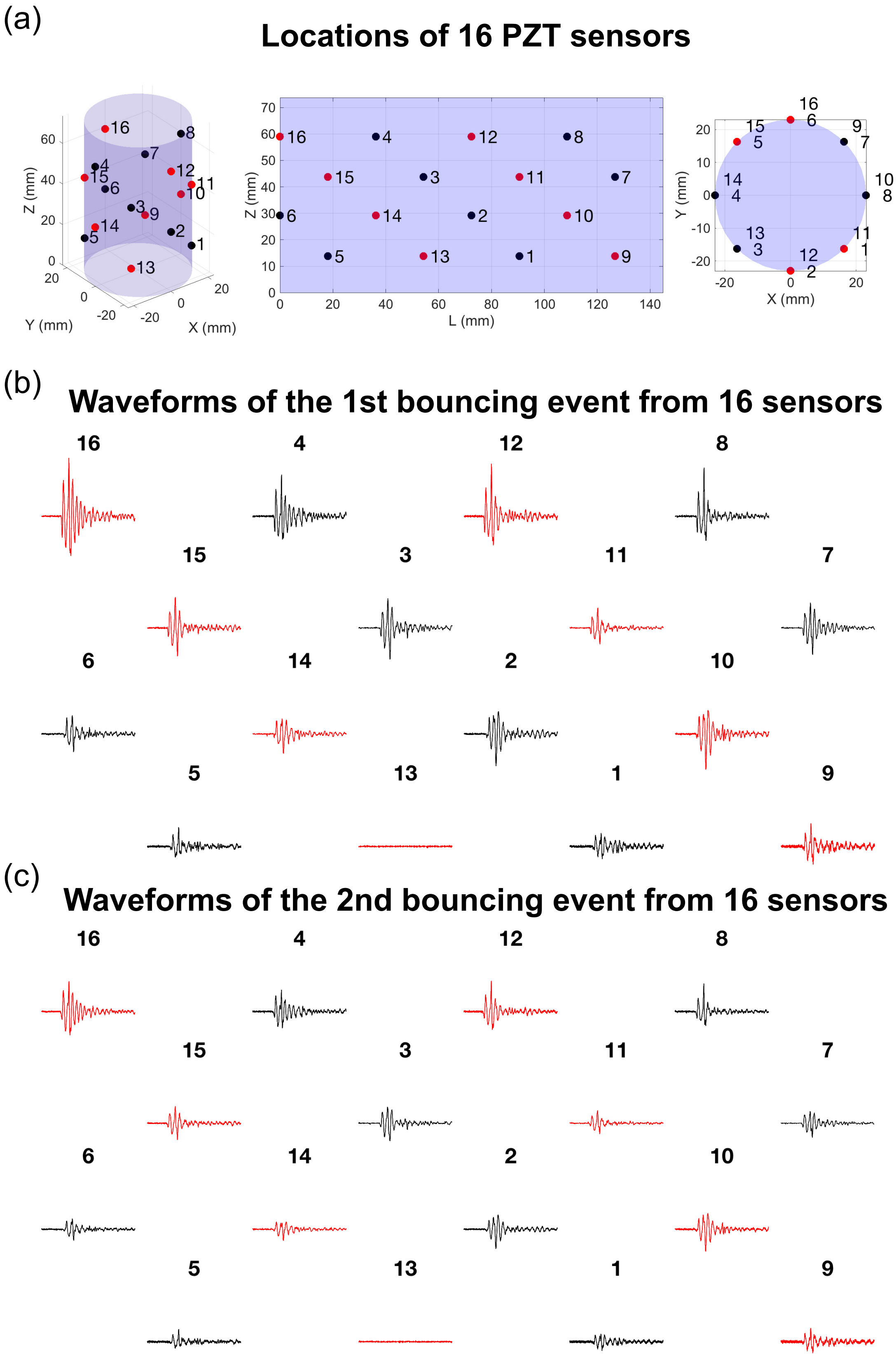

Figure 2. (a) Locations of 16 PZT sensors. (b) Example waveforms from 16 sensors for the 1st ball bounce.(b) Example waveforms from 16 sensors for the 2nd ball bounce. Black and red denote sensors and corresponding received signals on two different boards.

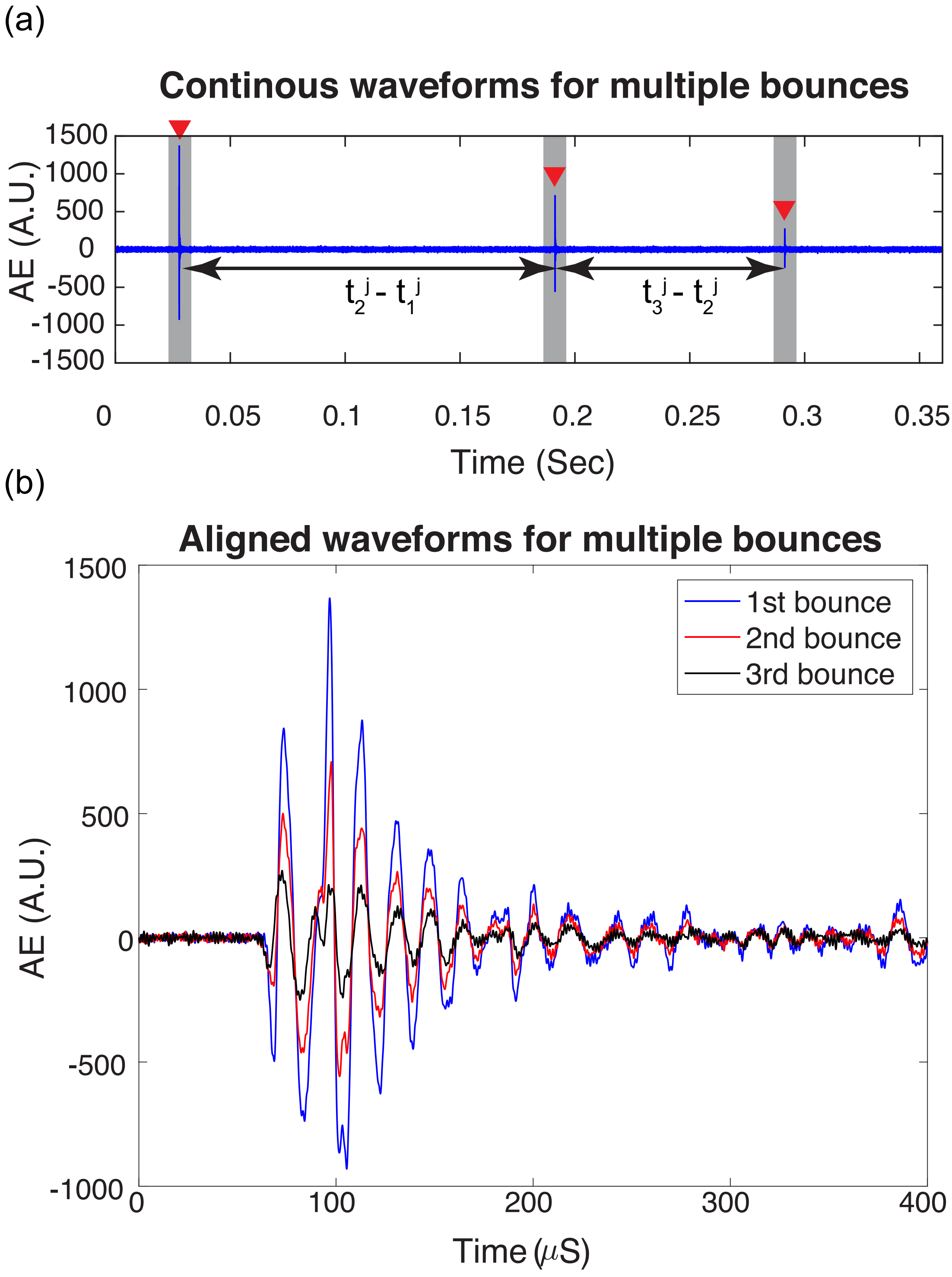

Figure 3. (a) Continuous waveforms containing the first three bouncing events of sensor 16. The grey shadow areas denote time windows of bouncing events used for cross-correlation. (b) Aligned waveforms of three continuous bouncing events of sensor 16.

The received waveform due to the kth ball bouncing can be written as

$$\boldsymbol{o}^{j,k}(t) = L[I[\boldsymbol{u}_i^{j,k}(\boldsymbol{x},t)]] = L[I[f_k(t) * \boldsymbol{G}(\boldsymbol{r_j},t)]], \tag{6}$$

where $\boldsymbol{o}^{j,k}(t)$ is the received waveform at receiver j, $\boldsymbol{u}_i^{j,k}(\boldsymbol{r_j},t)$ is the input displacement, $f_k(t)$ is the loading function of the kth bouncing of the ball, $\boldsymbol{G}(\boldsymbol{r_j},t)$ is the Green's function representing the impulsive response function of the sample at the receiver j, t is the time, $\boldsymbol{r_j}$ is the vector directed from the bouncing ball source to receiver j, I is the incident angle correction, and L is a linear operator, assuming that the response function of the PZT transducer can be modeled as a linear time-shift invariant (LTI) system. Based on previous studies of ball collisions (McLaskey & Glaser 2012; McLaskey et al. 2015), the loading function can be represented as

$$\begin{aligned} f_k(t) &= -F_{max,n} \sin\left(\frac{\pi t}{t_c}\right)^{3/2}, \quad 0 \le |t| \le t_c, \\ f_k(t) &= 0, \quad \text{otherwise}, \end{aligned} \tag{7}$$

where $F_{max,k}$ is the maximum loading force of the kth ball bouncing, and t_c is the total loading time, which is the entire contact time between the ball and the top surface of the sample. The $F_{max,i}$ and t_c are written as

$$F_{max,n} = 1.917\rho_1^{3/5}(\delta_1+\delta_2)^{-2/5}R_1^2 v_{k-1}^{6/5}, \tag{8}$$

$$\delta_q = \frac{1-\mu_q^2}{\pi E_q}, \quad q = 1,2 \tag{9}$$

$$t_c = 1/f_c = 4.53(4\rho_1\pi(\delta_1+\delta_2)/3)^{2/5}R_1 v_{k-1}^{-1/5}, \tag{10}$$

where ρ_q, E_q, μ_q are the density, Young's modulus, and Poisson's ratio of the qth material, respectively ($q = 1$ refers to the steel ball and $q = 2$ refers to the titanium sample). In this experiment, $\rho_1 = 8050\ kg/m^3$, $E_1 = 180.0\ GPa$, $\mu_1 = 0.305$, $\rho_2 = 4506\ kg/m^3$, $E_2 = 113.8\ GPa$, and $\mu_2 = 0.32$. v_{k-1} is the incident velocity of the kth bouncing of the ball.

$G_{i3}(\boldsymbol{r_j},t)$ is the ith ($i = 1,2,3$, corresponding to three axes) component of displacement at general $(\boldsymbol{x},t)$, for an impulsive point force source in the x_3 direction, i.e., vertical direction. The ith component of displacement due to the kth bounce $u_i^{j,k}(\boldsymbol{x},t)$ is represented as (Aki & Richards 2002)

$$\begin{aligned} u_i^{j,k}(\boldsymbol{x},t) =& f_k(t) * G_{i3}(\boldsymbol{r_j},t), \\ =& \frac{1}{4\pi\rho_2}(3\gamma_i^j\gamma_3^j - \delta_{i3})\frac{1}{r_j^3}\int_{\frac{r_j}{V_P}}^{\frac{r_j}{V_S}} \tau f_k(t-\tau)d\tau \\ &+ \frac{1}{4\pi\rho_2 V_P^2}\gamma_i^j\gamma_3^j\frac{1}{r_j}f_k\left(t-\frac{r_j}{V_P}\right) - \frac{1}{4\pi\rho_2 V_S^2}(\gamma_i^j\gamma_3^j - \delta_{i3})\frac{1}{r_j}f_k\left(t-\frac{r_j}{V_S}\right), \end{aligned} \tag{11}$$

where $V_P = 6011.6\ m/s$, and $V_S = 3093.0\ m/s$ are the P wave velocity and S wave velocity of the titanium sample, respectively; r_j is the norm of the vector from source to sensor j, γ_i^j is the directional cosine between r_j and the ith coordinate axis; δ_{i3} is the Kronecker delta function.

The incidence angle dependence of the sensor is assumed to be a cosine function, i.e.,

$$I[u_i^{j,k}(\boldsymbol{x},t)] = u_\perp^{j,k}(\boldsymbol{x},t) = u_i^{j,k}(\boldsymbol{x},t)\xi_i^j, \tag{12}$$

where ξ_i^j is the directional cosine of the normal vector of sensor j — $[r_1^j, r_2^j, 0]$.

The frequency-response function of sensor j is modeled by

$$\boldsymbol{R}^j(\omega) = \frac{-C\omega^2}{\omega^2 + 2i\varepsilon^j\omega - (\omega_s^j)^2}, \tag{13}$$

where ω_s^j is the resonance frequency, ε_s^j is the damping coefficient of sensor j, and C is the conversion constant with unit $count/m$.

Then, the noise-free signal at sensor j due to the kth bounce can be represented as

$$\boldsymbol{O}^{j,k}(\omega) = \boldsymbol{R}^j(\omega)\boldsymbol{U}_\perp^j(\omega) \tag{14}$$

in the frequency domain, and

$$\boldsymbol{o}^{j,k}(t) = \boldsymbol{r}^j(t) * \boldsymbol{u}_\perp^j(t) \tag{15}$$

in the time domain, where $*$ represents the convolution operator. Concatenating waveforms from all the bounces and noise perturbations $\boldsymbol{e}^{j,k}$, the data can be modeled as

$$\begin{bmatrix} \boldsymbol{d}^{j,1}(t) \\ \boldsymbol{d}^{j,2}(t) \\ \vdots \\ \boldsymbol{d}^{j,k}(t) \\ \vdots \\ \boldsymbol{d}^{j,n}(t) \end{bmatrix} = \begin{bmatrix} \boldsymbol{o}^{j,1}(t) \\ \boldsymbol{o}^{j,2}(t) \\ \vdots \\ \boldsymbol{o}^{j,k}(t) \\ \vdots \\ \boldsymbol{o}^{j,n}(t) \end{bmatrix} + \begin{bmatrix} \boldsymbol{e}^{j,1}(t) \\ \boldsymbol{e}^{j,2}(t) \\ \vdots \\ \boldsymbol{e}^{j,k}(t) \\ \vdots \\ \boldsymbol{e}^{j,n}(t) \end{bmatrix}, \tag{16}$$

which can be written more compactly as

$$\boldsymbol{d}^j(t) = \boldsymbol{o}^j(t) + \boldsymbol{e}^j(t). \tag{17}$$

2.3 Bayesian formulation and posterior sampling

In principle, one could use a Bayesian hierarchical model to represent the entire ball drop system, given bouncing time interval data $\boldsymbol{\delta t}$ and waveform data $\{\boldsymbol{d}^j\}_{j=1}^{16}$ from all sensors

$$\begin{aligned}&P\left(\{v_0^j, a^j, \omega_s^j, \varepsilon^j\}_{j=1}^{16}, v_0, a, \sigma_t^2 | \{\boldsymbol{d}^j\}_{j=1}^{16}, \boldsymbol{\delta t}\right)\\ \propto& P(\boldsymbol{\delta t}|v_0, a, \sigma_t^2)P(v_0)P(a)P(\sigma_t^2)\\ &\prod_{j=1}^{16} P(\boldsymbol{d}^j|v_0^j, a^j, \omega_s^j, \varepsilon^j) \prod_{j=1}^{16} P(v_0^j, a^j|v_0, a) \prod_{j=1}^{16} P(v_0^j)P(a^j)P(\omega_s^j)P(\varepsilon^j),\end{aligned} \tag{18}$$

where v_0 and a are master ball drop parameters given $\boldsymbol{\delta t}$, σ_t^2 is the variance hyperparameter, and v_0^j and a^j are ball drop parameters given waveform data $\{\boldsymbol{d}^j\}_{j=1}^{16}$, $P(\boldsymbol{\delta t}|v_0, a)$ and $P(\boldsymbol{d}^j|v_0^j, a^j, \omega_s^j, \varepsilon^j)$ are likelihood functions, and $P(v_0^j, a^j|v_0, a)$ is the probability distribution of v_0^j and a^j, given master v_0 and a. Here we use uniform probability distribution for $P(v_0)$, $P(a)$, $P(v_0^j)$, $P(a^j)$, $P(\omega_s^j)$, and $P(\varepsilon^j)$, that is,

$$\begin{aligned}&P(v_0) \sim \mathcal{U}(1.0, 1.5)m/s, \quad P(a), \sim \mathcal{U}(0.5, 0.9),\\ &P(v_0^j) \sim \mathcal{U}(1.0, 1.5)m/s, \quad P(a^j), \sim \mathcal{U}(0.5, 0.9),\\ &P(\omega_s^j) \sim \mathcal{U}(100, 500)kHz, \quad P(\varepsilon^j) \sim \mathcal{U}(10, 50)kHz,\end{aligned} \tag{19}$$

and normal distribution for σ_t^2, that is,

$$P(\sigma_t^2) \sim \mathcal{N}(10^{-10}, 10^{-20})s^2. \tag{20}$$

To simplify the sampling procedure, we ignore the difference between the master v_0 and a, and v_0^j and a^j, i.e., $P(v_0^j, a^j|v_0, a) \approx P(v_0^j, a^j)$; then we can sample $(\sigma_t^j)^2$ and $\boldsymbol{X} = [v_0^j, a^j, \omega_s^j, \varepsilon^j]$ for each sensor separately (Figure 4). For sensor j, the posterior probability density $P(v_0^j, a^j, \omega_s^j, \varepsilon^j, (\sigma_t^j)^2|\boldsymbol{d}^j)$ is written as

$$P(v_0^j, a^j, \omega_s^j, \varepsilon^j, (\sigma_t^j)^2|\boldsymbol{d}^j, \boldsymbol{\delta t}) \propto P((\sigma_t^j)^2)P(\boldsymbol{\delta t}|v_0^j, a^j, (\sigma_t^j)^2)P(\boldsymbol{d}^j|v_0^j, a^j, \omega_s^j, \varepsilon^j), \tag{21}$$

where the hyperprior distribution $P((\sigma_t^j)^2)$ is

$$P((\sigma_t^j)^2) \sim \mathcal{N}(10^{-10}, 10^{-20})s^2. \tag{22}$$

The likelihood functions $P(\boldsymbol{\delta t}|v_0^j, a^j)$ and $P(\boldsymbol{d}^j|v_0^j, a^j, \omega_s^j, \varepsilon^j)$ depend on the probability distributions $P_{e_t}(\boldsymbol{\delta t} - \boldsymbol{\delta t_m})$ and $P_{e^j}(\boldsymbol{d}^j - \boldsymbol{o}^j)$. In this paper, we assume both the errors are Gaussian, with the zero mean and diagonal covariance matrices $\boldsymbol{\Sigma_t}$ and $\boldsymbol{\Sigma}^j$.

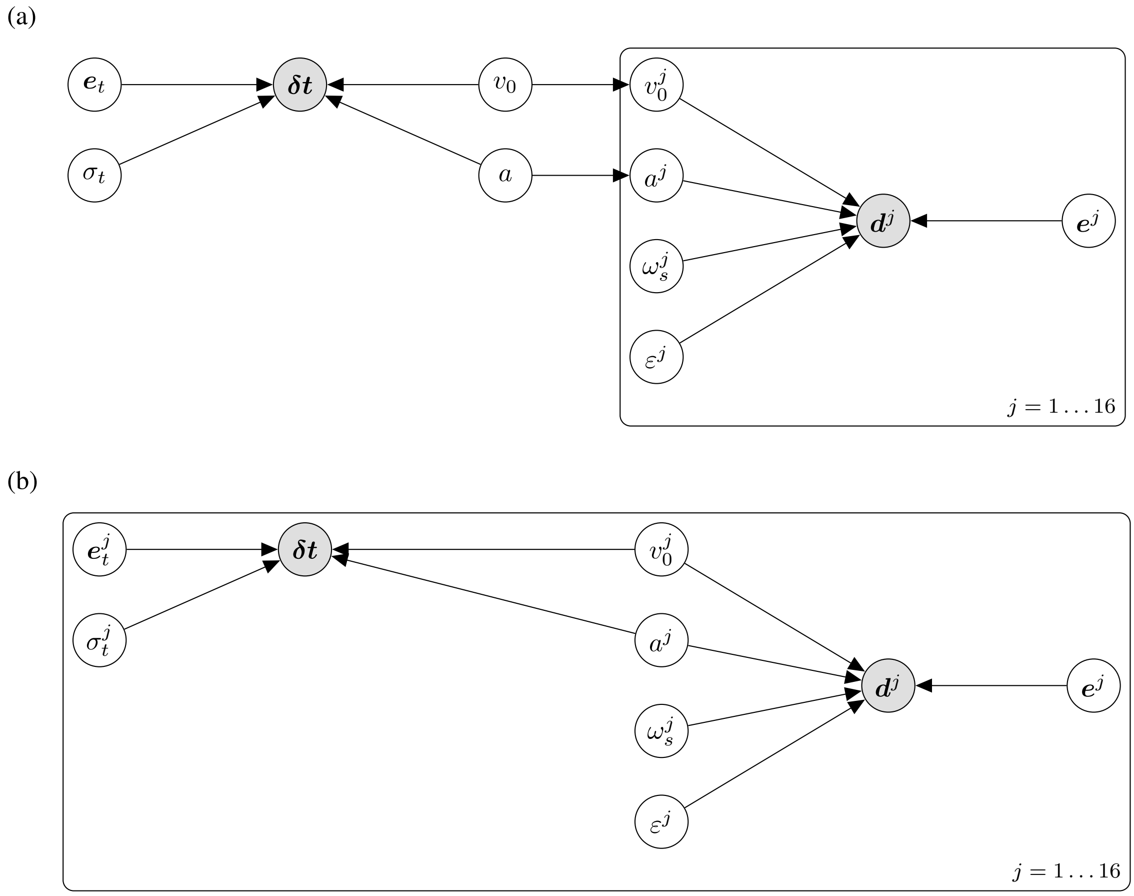

Figure 4. Schematic of simplified MCMC procedure. (a) The hierarchical model; (b) the decoupled model.

Then, the likelihood functions can be written as

$$P(\boldsymbol{\delta t}|v_0^j, a^j, (\sigma_t^j)^2) = \frac{1}{\sqrt{(2\pi)^{N_{\delta t}} \det \boldsymbol{\Sigma_t}}} \exp\left[-\frac{1}{2}(\boldsymbol{\delta t} - \boldsymbol{\delta t_m})^T \boldsymbol{\Sigma_t}^{-1} (\boldsymbol{\delta t} - \boldsymbol{\delta t_m})\right], \tag{23}$$

$$P(\boldsymbol{d}^j|v_0^j, a^j, \omega_s^j, \varepsilon^j) = \frac{1}{\sqrt{(2\pi)^N \det \boldsymbol{\Sigma}^j}} \exp\left[-\frac{1}{2}(\boldsymbol{d}^j - \boldsymbol{o}^j)^T (\boldsymbol{\Sigma}^j)^{-1} (\boldsymbol{d}^j - \boldsymbol{o}^j)\right]. \tag{24}$$

$\boldsymbol{\Sigma_t}$ and $\boldsymbol{\Sigma}^j$ are

$$\begin{aligned} &\boldsymbol{e_t} \sim \mathcal{N}(0, \boldsymbol{\Sigma_t}), \quad \Sigma_{t,ii} = \left(\sigma_t^j\right)^2, \quad i = 1, 2 \dots N_{\delta t}, \quad \text{and} \\ &\boldsymbol{e}^j \sim \mathcal{N}(0, \boldsymbol{\Sigma}^j), \quad \Sigma_{ii}^j = \left(\sigma^j\right)^2, \quad i = 1, 2 \dots N, \end{aligned} \tag{25}$$

where $N_{\delta t}$ and N are the total number of data samples for waveforms $\boldsymbol{d}^j$ and bouncing time interval $\boldsymbol{\delta t}$. $(\sigma_t^j)^2$ is sampled by Equation 22, and $\left(\sigma^j\right)^2$ is $\alpha^j \in (0, 1)$ of the power of waveform data $\boldsymbol{d}^j$, that is,

$$\left(\sigma^j\right)^2 = \alpha^j \frac{1}{T} \int_0^T d^2(t) dt \approx \alpha^j \frac{1}{T} \sum_{i=1}^{N} \Delta t (d_i^j)^2 = \alpha^j \frac{1}{N} \sum_{i=1}^{N} (d_i^j)^2, \tag{26}$$

where T is the total time length of waveform data and N is the number of total samples. α^j, the ratio of noise and waveform data power for sensor j, is estimated by

$$\alpha^j = \frac{\frac{1}{T_e}\int_0^{T_e} e^2(t)dt}{\frac{1}{T}\int_0^{T} d^2(t)dt} \approx \frac{\frac{1}{T_e}\sum_{i=1}^{N_e} \Delta t(e_i^j)^2}{\frac{1}{T}\sum_{i=1}^{N} \Delta t(d_i^j)^2} = \frac{N\sum_{i=1}^{N_e}(e_i^j)^2}{N_e\sum_{i=1}^{N_e}(d_i^j)^2}, \tag{27}$$

where T_e is the time length of the noise window (the time window before the first P arrival of the first bouncing event) and and N_e is the number of noise samples. Substituting α^j in Equation 26 by Equation 27, we obtain

$$\left(\sigma^j\right)^2 = \frac{1}{N_e}\sum_{i=1}^{N_e}(e_i^j)^2. \tag{28}$$

We use the adaptive Metropolis (AM) Markov chain Monte Carlo (MCMC) sampling method to characterize the posterior distribution of $\boldsymbol{X}$ (Metropolis et al. 1953; Hastings 1970; Haario et al. 2001). The AM scheme, a particular MCMC scheme, adjusts the covariance matrix of the Metropolis proposal distribution after each step of the MCMC chain, based on all previous samples of $\boldsymbol{X}$:

$$C^*_{n_0} = s_d\,\mathrm{Cov}(\boldsymbol{X}_0, \ldots, \boldsymbol{X}_{n_0}) + s_d\epsilon_0 I_d\,. \tag{29}$$

Here $C^*_{n_0}$ is the updated proposal covariance matrix at step n_0, I_d is the d-dimensional identity matrix, $\epsilon_0 > 0$ is a small constant to make $C^*_{n_0}$ positive definite, $d = 4$ is the dimension of $\boldsymbol{X}$, and $s_d = 2.4^2/d$. The value of the scaling parameter s_d is a standard choice to optimize the mixing properties of the Metropolis search (Gelman et al. 1996). This value might affect the efficiency of MCMC, but not the posterior distribution itself.

3 RESULTS AND DISCUSSION

We apply the Bayesian method to all 16 sensors (sensor 13 did not work during the experiment). For each sensor, we calculate the parameter α^j based on Equation 27. We perform 10^6 MCMC iterations for each sensor. The first 6×10^5 iterations of MCMC chains are discarded as burn-in. The values of α^j for 16 sensors are shown in Table 1. The sensors at the top half of the cylinder sample (sensors 16, 4, 12, 8, 15, 3, 11, 7), which are closer to the ball bouncing source, generally have lower α^j than sensors at the bottom half of the cylinder sample, e.g., sensors 6, 14, 2, 10, 5, 13, 1, 9. This is because the sensors close to the source have better signal-to-noise ratio compared to sensors away from the source. α^j is an indicator of signal quality.

We show MCMC chains and posterior distributions of v_0^j, a^j, ω_s^j, and ε^j for sensor 16 in Figures 5(a) and (b). Figure 5(c) shows the mean posterior predicted trajectory of ball bouncing events.

The comparison between the observed AE data and mean posterior predicted waveforms is shown in Figure 5(d).

Posterior distribution and uncertainties of $(\sigma_t^2)^j$, v_0^j, a^j, ω_s^j, and ε^j are summarized in Table 1. Sensors closer to the bouncing source have higher standard deviation than sensors farther away from the bouncing source.

Figure 6(a) shows the comparison between observed and mean posterior predicted bouncing time intervals, $t_2^j - t_1^j$ and $t_3^j - t_2^j$, for all the sensors. The bias is smaller than $20\mu S$. Figure 6(b) shows the comparison between observed and mean posterior predicted waveforms. The observed waveforms are all well predicted. Blue and light blue shading areas show the 1σ and 2σ regions of posterior predicted waveforms after the burn-in. The 2σ region of post-burn-in predicted waveforms (light blue shadow areas) almost covers the observed waveforms. The higher the noise levels of the observations, the larger the light blue shadow areas. In contrast, the sensors with high signal quality generally show larger bias in bouncing time intervals. This is probably because of the trade-off between the likelihood functions $P(\boldsymbol{\delta t}|v_0^j, a^j)$ and $P(\boldsymbol{d}^j|v_0^j, a^j, \omega_s^j, \varepsilon^j)$.

The mean posterior predicted resonance frequency ω_s^j for all different sensors varies from 311 to 364 kHz, and the damping coefficient ε^j varies from 13 to 40 kHz. The posterior standard deviations for ω_s^j and ε^j are all within 1 kHz. With the posterior predicted ω_s^j and ε^j, we can obtain frequency-response functions of all sensors by Equation 13(a). The standard deviation indicates how reliable the response function of each sensor is. We show the mean posterior amplitude response and phase delay of all response functions in Figure 7(a). The amplitude response tends to a constant at high frequencies, and is proportional to ω^2 at low frequencies. The phase delay is close to zero at low frequencies and tends to π at high frequencies. The $in\ situ$ response functions can be used to calibrate real AE data under high pressure conditions.

We plot ω_s^j and ε^j as a function of source-receiver distance in Figure 7(b). ω_s^j shows a clear trend of decay with the increasing source-receiver distance, indicating that attenuation effects, which are not included in our model, should be taken into account in Equation 11 to avoid mapping sample Q into instrument response functions. ε^j does not show any distance-dependent properties.

4 CONCLUSION

We develop a Bayesian waveform-based method to calibrate PZT sensors of a newly designed $in\ situ$ ball drop system in a sealed pressure vessel. Taking full waveforms due to ball bounces as input data, the Bayesian method successfully obtains posterior distributions of model parameters v_0^j, a^j, ω_s^j, and ε^j. Both the posterior distributions of $in\ situ$ response functions of PZT sensors and the trajectories of ball bounces are recovered by this method.

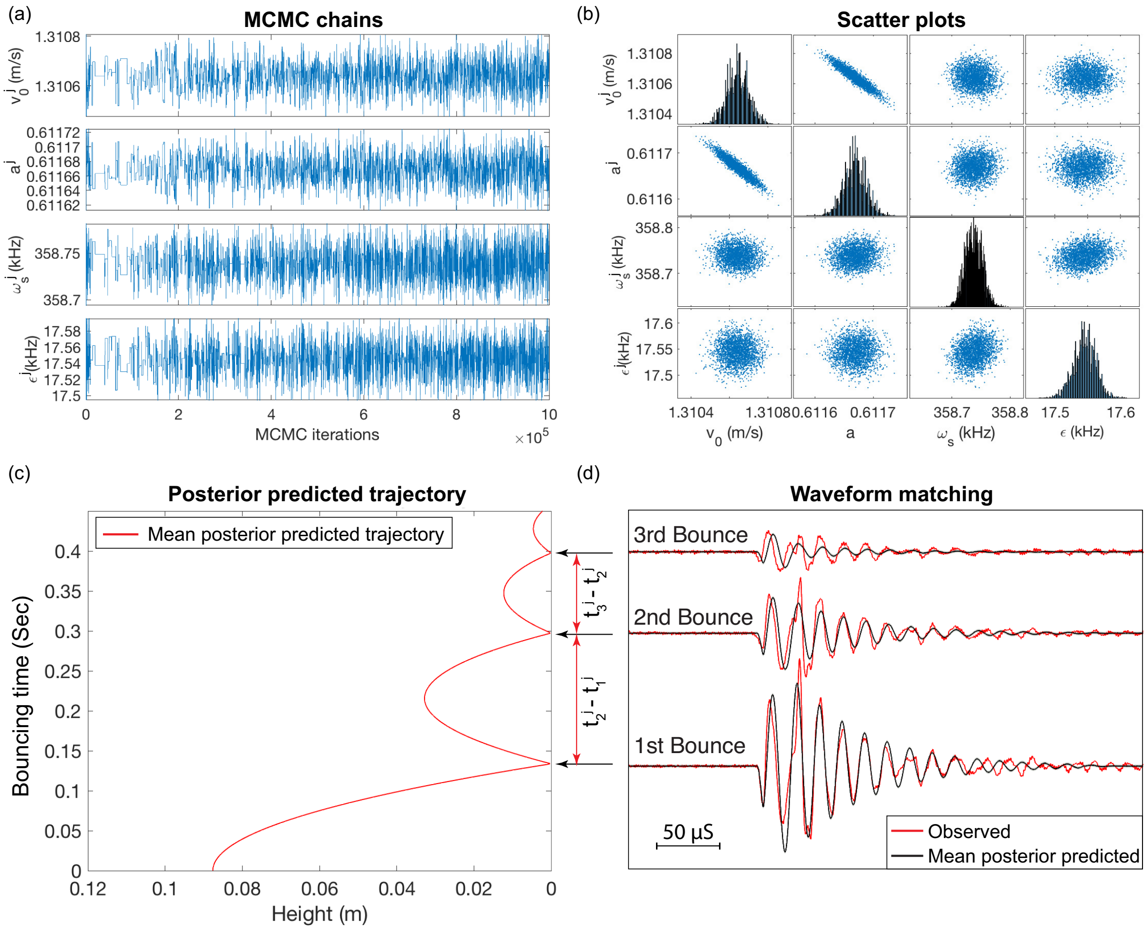

Figure 5. MCMC chains and posterior distribution of four parameters for sensor 16. The first 6×10^5 iterations of MCMC chains are discarded as burn-in. (a) MCMC chains for initial velocity v_0^j, rebound coefficient a^j, resonance frequency ω_s^j, and damping coefficient ε^j. (b) Scatter plots of four parameters corresponding to MCMC chains. (c) Mean posterior predicted trajectory of ball bouncing. (d) Waveform comparison between observed (red) and mean posterior predicted waveforms (black).

With the $in\ situ$ estimation of frequency-dependent sensor response functions, we are able to convert the AE waveforms' amplitude and phase to a real physical parameter (e.g., displacements or accelerations) under high pressure conditions. The obtained uncertainties of response functions indicate the reliability of each sensor.

Our proposed method was tested on a titanium cylinder, with a very homogeneous structure; but for more complex (and realistic) cases, additional work needs to be performed. A good estimate of wave speeds is required, and, for example, attenuation in other rock types can be significant (Lockner et al. 1977; Winkler et al. 1979) and, as shown in Figure 7(b), may be mapped into instrument response if not accounted for. We believe that using multiple bounces will allow for a better constraint of the attenuation of the sample as well as for estimating wave speeds using relative arrival times and cross-

Table 1. Posterior mean and standard deviation (std dev) of $(\sigma_t^j)^2$, v_0^j, a^j, ω_s^j, and ε^j for 16 sensors.

ID	α^j	$(\sigma_t^j)^2$ $(10^{-10}s^2)$		v_0^j (m/s)		a^j		ω_s^j (kHz)		ε^j (kHz)	
		mean	std dev	mean	std dev	mean	std dev	mean	std dev	mean	std dev
1	0.103	0.917	0.074	1.31100	5E-5	0.61152	2E-5	321.48	0.15	12.93	0.11
2	0.013	0.918	0.074	1.31115	5E-5	0.61147	2E-5	330.47	0.03	18.26	0.03
3	0.005	0.917	0.074	1.31130	5E-5	0.61144	2E-5	338.42	0.02	22.00	0.03
4	0.012	0.916	0.074	1.31102	5E-5	0.61152	2E-5	364.67	0.04	22.77	0.04
5	0.074	0.917	0.074	1.31103	5E-5	0.61151	2E-5	323.93	0.17	34.76	0.17
6	0.030	0.918	0.074	1.31104	5E-5	0.61151	2E-5	311.61	0.08	31.06	0.10
7	0.006	0.918	0.075	1.31122	6E-5	0.61146	2E-5	339.36	0.02	15.50	0.02
8	0.014	0.918	0.074	1.31102	5E-5	0.61152	2E-5	356.53	0.08	40.51	0.09
9	0.085	0.918	0.074	1.31103	5E-5	0.61151	2E-5	333.22	0.11	23.96	0.14
10	0.012	0.918	0.074	1.31128	5E-5	0.61143	2E-5	335.74	0.03	17.36	0.03
11	0.016	0.918	0.074	1.31111	5E-5	0.61149	2E-5	347.06	0.07	34.66	0.08
12	0.013	0.917	0.074	1.31116	5E-5	0.61147	2E-5	347.68	0.06	26.62	0.06
13	-	-	-	-	-	-	-	-	-	-	-
14	0.021	0.919	0.074	1.31110	5E-5	0.61149	2E-5	319.47	0.05	19.52	0.05
15	0.012	0.918	0.074	1.31101	5E-5	0.61152	2E-5	335.04	0.05	30.65	0.05
16	0.004	0.917	0.073	1.31064	5E-5	0.61167	2E-5	358.74	0.01	17.55	0.02

correlation methods (Waldhauser & Ellsworth 2000; Zhang & Thurber 2003; Fuenzalida et al. 2013; Weemstra et al. 2013).

ACKNOWLEDGMENTS

This research was supported by Total, Shell Global, and MIT Earth Resources Laboratory.

REFERENCES

Aki, K. & Richards, P. G., 2002. *Quantitative seismology*.

Drouillard, T., 1987. Introduction to acoustic emission technology, *Nondestructive testing handbook*, **5**.

Drouillard, T., 1996. A history of acoustic emission, *Journal of acoustic emission*, **14**(1), 1–34.

Earle, P. S. & Shearer, P. M., 1994. Characterization of global seismograms using an automatic-picking algorithm, *Bulletin of the Seismological Society of America*, **84**(2), 366–376.

Fu, W., Ames, B., Bunger, A., Savitski, A., et al., 2015. An experimental study on interaction between hy-

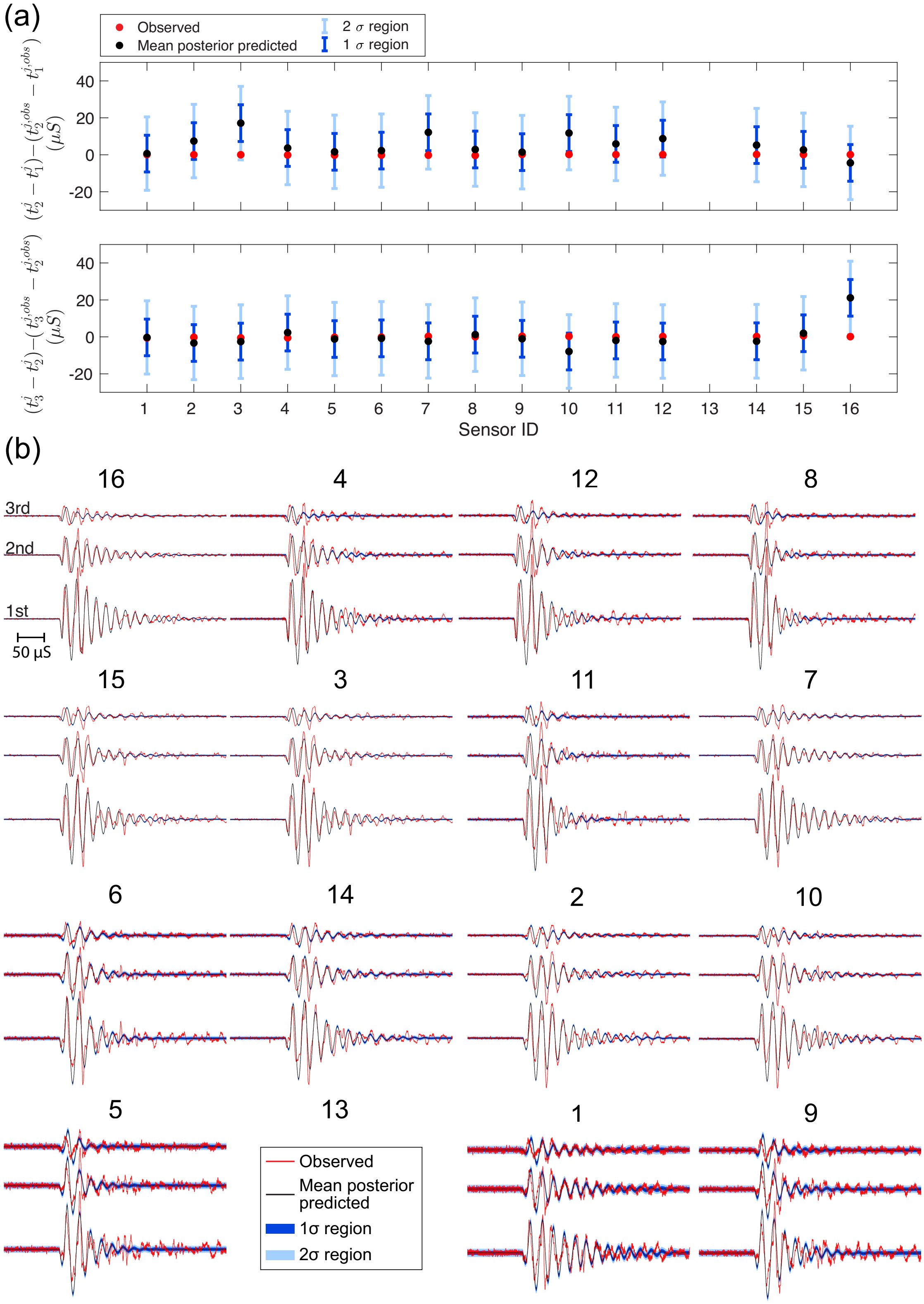

Figure 6. (a) Comparison between observed (red) and mean posterior predicted (blue) bouncing time intervals. The error bars indicate the 1σ and 2σ regions. (b) Waveform comparison between observed (red) and mean posterior predicted (black) waveforms of three bouncing events for 16 PZT sensors. Blue and light blue shading areas show the 1σ and 2σ regions of posterior predicted waveforms after the burn-in. The title of each subplot denotes sensor ID. Subplots are arranged in the order of sensor locations shown in Figure 2. Sensor 13 did not work, so we put the legend in the position of sensor 13.

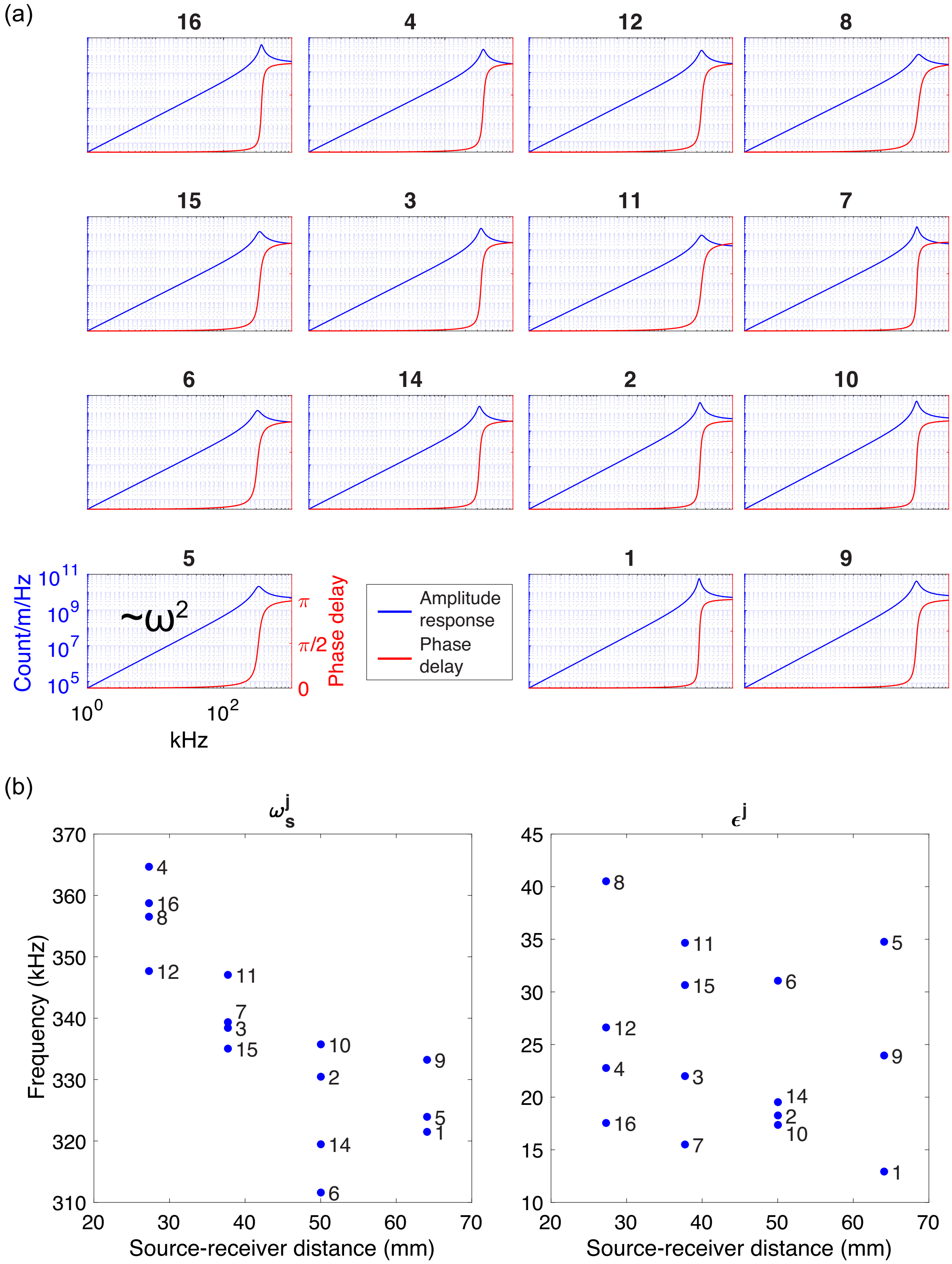

Figure 7. (a) Mean posterior predicted amplitude response (blue) and phase delay (red). The amplitude response tends to a constant at high frequencies, and is proportional to ω^2 at low frequencies. The title of each subplot denotes sensor ID. Subplots are arranged in the order of sensor locations shown in Figure 2. Sensor 13 did not work, so we put the legend in the position of sensor 13. (b) ω_s^j and ε^j as a function of source-receiver distance.

draulic fractures and partially-cemented natural fractures, in *49th US Rock Mechanics/Geomechanics Symposium*, American Rock Mechanics Association.

Fuenzalida, A., Schurr, B., Lancieri, M., Sobiesiak, M., & Madariaga, R., 2013. High-resolution relocation and mechanism of aftershocks of the 2007 tocopilla (chile) earthquake, *Geophysical Journal International*, **194**(2), 1216–1228.

Gelman, A., Roberts, G. O., Gilks, W. R., et al., 1996. Efficient metropolis jumping rules, *Bayesian statistics*, **5**(599-608), 42.

Goodfellow, S., Nasseri, M., Maxwell, S., & Young, R., 2015. Hydraulic fracture energy budget: Insights from the laboratory, *Geophysical Research Letters*, **42**(9), 3179–3187.

Graham, C., Stanchits, S., Main, I., & Dresen, G., 2010. Comparison of polarity and moment tensor inversion methods for source analysis of acoustic emission data, *International journal of rock mechanics and mining sciences*, **47**(1), 161–169.

Grosse, C. U. & Ohtsu, M., 2008. *Acoustic emission testing*, Springer Science & Business Media.

Haario, H., Saksman, E., & Tamminen, J., 2001. An adaptive metropolis algorithm, *Bernoulli*, pp. 223–242.

Hampton, J., Matzar, L., Hu, D., Gutierrez, M., et al., 2015. Fracture dimension investigation of laboratory hydraulic fracture interaction with natural discontinuity using acoustic emission, in *49th US Rock Mechanics/Geomechanics Symposium*, American Rock Mechanics Association.

Hastings, W. K., 1970. Monte carlo sampling methods using markov chains and their applications, *Biometrika*, **57**(1), 97–109.

Kaiser, E., 1950. A study of acoustic phenomena in tensile test, *Dr.-Ing. Dissertation. Technical University of Munich*.

Kurz, J. H., Grosse, C. U., & Reinhardt, H.-W., 2005. Strategies for reliable automatic onset time picking of acoustic emissions and of ultrasound signals in concrete, *Ultrasonics*, **43**(7), 538–546.

Kwiatek, G., Goebel, T., & Dresen, G., 2014. Seismic moment tensor and b value variations over successive seismic cycles in laboratory stick-slip experiments, *Geophysical Research Letters*, **41**(16), 5838–5846.

Li, B. Q. & Einstein, H. H., 2017. Comparison of visual and acoustic emission observations in a four point bending experiment on barre granite, *Rock Mechanics and Rock Engineering*, **50**(9), 2277–2296.

Lockner, D., Walsh, J., & Byerlee, J., 1977. Changes in seismic velocity and attenuation during deformation of granite, *Journal of Geophysical Research*, **82**(33), 5374–5378.

Maeda, N., 1985. A method for reading and checking phase times in auto-processing system of seismic wave data, *Zisin= Jishin*, **38**(3), 365–379.

McEvilly, T. & Majer, E., 1982. Asp: An automated seismic processor for microearthquake networks, *Bulletin of the Seismological Society of America*, **72**(1), 303–325.

McLaskey, G. C. & Glaser, S. D., 2012. Acoustic emission sensor calibration for absolute source measurements, *Journal of Nondestructive Evaluation*, **31**(2), 157–168.

McLaskey, G. C., Lockner, D. A., Kilgore, B. D., & Beeler, N. M., 2015. A robust calibration technique for acoustic emission systems based on momentum transfer from a ball drop, *Bulletin of the Seismological*

Society of America, **105**(1), 257–271.

Metropolis, N., Rosenbluth, A. W., Rosenbluth, M. N., Teller, A. H., & Teller, E., 1953. Equation of state calculations by fast computing machines, *The journal of chemical physics*, **21**(6), 1087–1092.

Obert, L. & Duvall, W., 1942. Use of subaudible noises for the prediction of rock bursts, part ii, us bur, *Mines Rep*, **3654**.

Ojala, I. O., Main, I. G., & Ngwenya, B. T., 2004. Strain rate and temperature dependence of omori law scaling constants of ae data: Implications for earthquake foreshock-aftershock sequences, *Geophysical Research Letters*, **31**(24).

Ono, K., 2016. Calibration methods of acoustic emission sensors, *Materials*, **9**(7), 508.

Pettitt, W. S., 1998. *Acoustic emission source studies of microcracking in rock.*, Ph.D. thesis, University of Keele.

Schofield, B., 1961. Acoustic emission under applied stress, Tech. Rep. ARL-150, Lessels and Associates, Boston.

Stanchits, S., Mayr, S., Shapiro, S., & Dresen, G., 2011. Fracturing of porous rock induced by fluid injection, *Tectonophysics*, **503**(1), 129–145.

Swindell, W. & Snell, N., 1977. Station processor automatic signal detection system, phase i: Final report, station processor software development, *Texas Instruments Report No. ALEX (01)-FR-77-01, AFTAC Contract Number FO8606-76-C-0025, Texas Instruments Incorporated, Dallas, Texas*.

W Goebel, T., Schorlemmer, D., Becker, T., Dresen, G., & Sammis, C., 2013. Acoustic emissions document stress changes over many seismic cycles in stick-slip experiments, *Geophysical Research Letters*, **40**(10), 2049–2054.

Waldhauser, F. & Ellsworth, W. L., 2000. A double-difference earthquake location algorithm: Method and application to the northern hayward fault, california, *Bulletin of the Seismological Society of America*, **90**(6), 1353–1368.

Weemstra, C., Boschi, L., Goertz, A., & Artman, B., 2013. Seismic attenuation from recordings of ambient noiseattenuation from ambient noise, *Geophysics*, **78**(1), Q1–Q14.

Winkler, K., Nur, A., & Gladwin, M., 1979. Friction and seismic attenuation in rocks, *Nature*, **277**(5697), 528.

Yoshimitsu, N., Furumura, T., & Maeda, T., 2016. Geometric effect on a laboratory-scale wavefield inferred from a three-dimensional numerical simulation, *Journal of Applied Geophysics*, **132**, 184–192.

Zhang, H. & Thurber, C. H., 2003. Double-difference tomography: The method and its application to the hayward fault, california, *Bulletin of the Seismological Society of America*, **93**(5), 1875–1889.

APPENDIX A: WAVEFORMS AFTER THE 3RD BOUNCING EVENT

In the main text, we only use waveform data for the first three bounces. We show the complete continuous waveforms containing waveforms after the third bounce event for 16 sensors in Figure A1. The expected fourth bouncing event, marked as a dashed triangle, does not appear around the theoretical

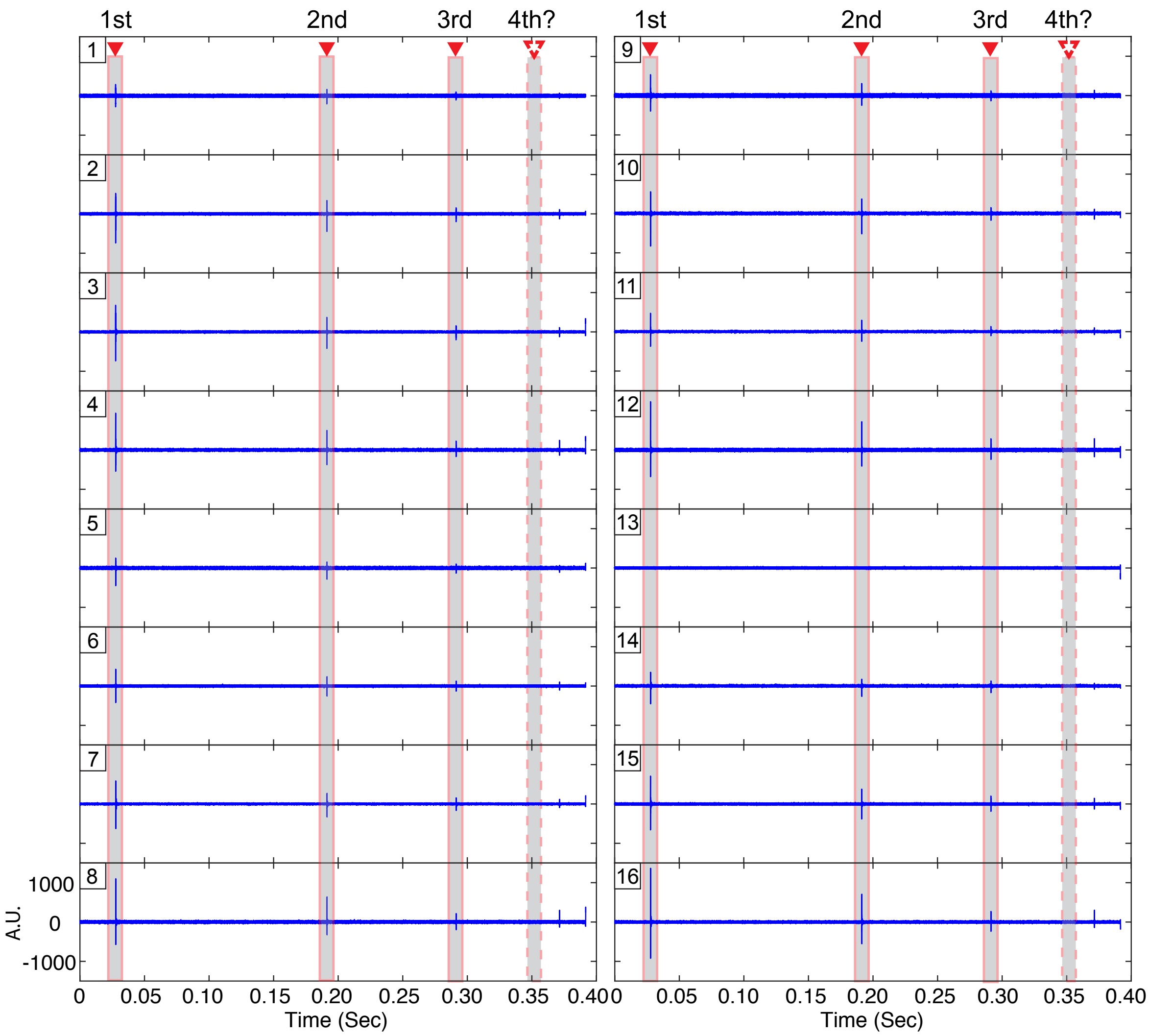

Figure A1. Complete continuous waveforms containing waveforms after the 3rd bounce event for 16 sensors. The first three bouncing events are denoted as solid red triangles. The dashed triangle marks the theoretical arrival time of bounces based on Equation 4.

time, but around 0.2 sec later. The fourth bouncing event even presents higher amplitude than the third bouncing event at sensor 4, 8, 12 and 16. This indicates that after the third bounce, when the rebound vertical velocity becomes 21.6% of the initial velocity v_0 and the maximum rebound height becomes 4.9 mm (comparable to the radius of the ball 3.18 mm), the simple rebound model cannot predict the ball's motion. The inclusion of other forces neglected in the main text, e.g., the drag force due to air resistance, and the Magnus force due to the ball's spin, and the buoyant force, may help to improve the simple rebound model and predict the ball's trajectory after the third bounce; however, that is beyond the scope of this paper.